Unveiling the ice and gas nature of active centaur (2060) Chiron using the James Webb Space Telescope

N. Pinilla-Alonso, J. Licandro, R. Brunetto, E. Henault, C. Schambeau, A. Guilbert-Lepoutre, J. Stansberry, I. Wong, J. I. Lunine, B. J. Holler, et al.

▶ **To cite this version:**

N. Pinilla-Alonso, J. Licandro, R. Brunetto, E. Henault, C. Schambeau, et al.. Unveiling the ice and gas nature of active centaur (2060) Chiron using the James Webb Space Telescope. Astronomy & Astrophysics, 2024, 692, 10.1051/0004-6361/202450124 . insu-04858908

HAL Id: insu-04858908

https://insu.hal.science/insu-04858908v1

Submitted on 30 Dec 2024

HAL is a multi-disciplinary open access archive for the deposit and dissemination of scientific research documents, whether they are published or not. The documents may come from teaching and research institutions in France or abroad, or from public or private research centers.

L'archive ouverte pluridisciplinaire **HAL**, est destinée au dépôt et à la diffusion de documents scientifiques de niveau recherche, publiés ou non, émanant des établissements d'enseignement et de recherche français ou étrangers, des laboratoires publics ou privés.

Distributed under a Creative Commons Attribution 4.0 International License

A&A 692, L11 (2024)
https://doi.org/10.1051/0004-6361/202450124
© The Authors 2024

Astronomy & Astrophysics

LETTER TO THE EDITOR

Unveiling the ice and gas nature of active centaur (2060) Chiron using the *James Webb* Space Telescope

N. Pinilla-Alonso[1,2,⋆], J. Licandro[3,4], R. Brunetto[5], E. Henault[5], C. Schambeau[2,6], A. Guilbert-Lepoutre[7], J. Stansberry[8,9,10], I. Wong[11,12], J. I. Lunine[13], B. J. Holler[8], J. Emery[9], S. Protopapa[14], J. Cook[14], H. B. Hammel[15], G. L. Villanueva[11], S. N. Milam[11], D. Cruikshank[6], and A. C. de Souza-Feliciano[2]

[1] Institute for Space Sciences and Technologies in Asturias (ICTEA), University of Oviedo, Oviedo, Spain
[2] Florida Space Institute, University of Central Florida, Orlando, FL, USA
[3] Instituto Astrofísico de Canarias, La Laguna, Tenerife, Spain
[4] Universidad de La Laguna, Tenerife, Spain
[5] Université Paris-Saclay, CNRS, Institut d'Astrophysique Spatiale, Orsay, France
[6] University of Central Florida, Physics Department, Orlando, FL, USA
[7] Laboratoire de Géologie de Lyon: Terre, Planètes, Environnement, UMR 5276 CNRS, UCBL, ENSL, Villeurbanne, France
[8] Space Telescope Science Institute, Baltimore, MD, USA
[9] Northern Arizona University, Flagstaff, AZ, USA
[10] Lowell Observatory, Flagstaff, AZ, USA
[11] NASA Goddard Space Flight Center, Greenbelt, MD, USA
[12] American University, Washington, DC, USA
[13] Cornell University, Department of Astronomy, Ithaca, NY, USA
[14] Southwest Research Institute, Boulder, CO, USA
[15] Association of Universities for Research in Astronomy, Washington, DC, USA

Received 25 March 2024 / Accepted 25 June 2024

ABSTRACT

Context. (2060) Chiron is a large centaur that has been reported active on multiple occasions at relatively large heliocentric distances, including during aphelion passage. Studies of Chiron's coma during active periods have resulted in the detection of C≡N and CO outgassing. Additionally, Chiron is surrounded by a disk of debris that varies with time. Significant work remains to be undertaken to comprehend the activation mechanisms on Chiron and the parent molecules of the gas phases detected.

Aims. This work reports the study of the ices on Chiron's surface and coma and seeks spectral indicators of volatiles associated with the activity. Additionally, we discuss how these detections could be related to the activation mechanism for Chiron and, potentially, other centaurs.

Methods. In July 2023, the *James Webb* Space Telescope (JWST) observed Chiron when it was active near its aphelion. We present JWST/NIRSpec spectra from 0.97 to 5.27 μm with a resolving power of ~1000, and compare them with laboratory data for identification of the spectral bands.

Results We report the first detections on Chiron of absorption bands of several volatile ices, including CO_2, CO, C_2H_6, C_3H_8, and C_2H_2. We also confirm the presence of water ice in its amorphous state. A key discovery arising from these data is the detection of fluorescence emissions of CH_4, revealing the presence of a gas coma rich in this hyper-volatile molecule, which we also identify to be in non-local thermal equilibrium (non-LTE). CO_2 gas emission is also detected in the fundamental stretching band at 4.27 μm. We argue that the presence of CH_4 emission is the first proof of the desorption of CH_4 due to a density phase transition of amorphous water ice at low temperature in agreement with the estimated temperature of Chiron during the JWST observations (61 K). Detection of photolytic and proton irradiation products of CH_4 and CO_2 on the surface, in the coma ice grains, or in the ring material is also detected via a forest of absorption features from 3.5 to 5.3 μm.

Key words. techniques: spectroscopic – comets: general – Kuiper belt objects: individual: (2060) Chiron

1. Introduction

(2060) Chiron, Chiron hereafter, a large centaur with a diameter of approximately 215.6 km and a *V*-band geometric albedo of 0.16 Fornasier et al. (2013), displays sporadic brightness increases attributed to episodes of enhanced dust production or sublimation at distances ranging from 8.5 to 18.8 au (Tholen 1988; Marcialis & Buratti 1993; Lazzaro et al. 1997). A recent outburst in 2021, as Chiron approached aphelion, resulted in a brightness increase of at least 0.6 mag, although its activity level has since decreased by more than 50% in terms of brightness (Dobson et al. 2021; Ortiz et al. 2023).

Commonly associated with the presence of volatile ices in their interior or coma, activity in centaurs is a complex phenomenon that remains to be fully comprehended. Spectroscopy of Chiron's surface at $\lambda < 2.2$ μm has not definitively revealed its ice content, but broad absorption bands at 1.5 and 2.02 μm

⋆ Corresponding author; npinilla@ucf.edu

Open Access article, published by EDP Sciences, under the terms of the Creative Commons Attribution License (https://creativecommons.org/licenses/by/4.0), which permits unrestricted use, distribution, and reproduction in any medium, provided the original work is properly cited.
This article is published in open access under the Subscribe to Open model. Subscribe to A&A to support open access publication.

suggest water ice mixed with dust, forming a low-albedo, volatile-ice-poor mantle (Luu et al. 2000). In contrast, the search for gases in the coma during active periods revealed a more exotic nature. Bus et al. (1991) reported C≡N outgassing on Chiron at a heliocentric distance of 11.3 au, attributing that emission to a recent CO2 outburst. Womack & Stern (1999) detected CO molecules in Chiron's coma close to its perihelion passage (r = 8.5 au), proposing sublimation of CO ice as the agent generating Chiron's activity. In 2015, Ortiz et al. (2015) reported the discovery of an unevenly distributed ring of debris encircling Chiron. Recent observations suggest its material is highly variable (Sickafoose et al. 2023; Ortiz et al. 2023), though its relationship to surface outbursts remains uncertain.

James Webb Space Telescope (JWST) observations of inactive centaurs have revealed diverse surface compositions, detecting molecules such as H_2O, CO_2, CH_3OH, C≡N, and OCS (Licandro et al. 2024). Notably, CO, prevalent in about 55% of the trans-Neptunian objects (TNOs) observed by DiSCo-TNOs (Pinilla-Alonso et al. 2024; De Prá et al. 2024)), is depleted on inactive centaurs due to sublimation at the higher surface temperatures in the giant planet region. Additionally, detections of light hydrocarbons (CH_4, C_2H_2, C_2H_4, C_2H_6, etc.) common in protoplanetary disks have been reported for TNOs larger than 1000 km (Emery et al. 2024). Here, we report detections of ice and gas species on Chiron using a JWST/NIRSpec spectrum (0.97–5.27 μm) acquired in 2023, approximately two years after its last activity outburst.

2. Observations and data reduction

The JWST observed Chiron using the integral field unit (IFU) of the Near-Infrared Spectrograph (NIRSpec, Jakobsen et al. 2022; Böker et al. 2023). After standard processing via the calibration pipeline, the IFU spectral cubes consist of 3″-square images at different wavelengths, enabling both compositional and morphological studies. The data were taken as part of the Cycle 1 Guaranteed Time Observations (GTO) Program 1273 (PI: J. Lunine). Observations were carried out on UT July 12, 2023 when Chiron was at 18.771 au from the Sun, using three grating-filter combinations: G140M/F100LP (0.97–1.89 μm), G235M/F140LP (1.66–3.17 μm), and G395M/F290LP (2.87—5.27 μm), which provide a spectral resolving power of R ∼ 1000. The observations spanned the period from UT 9:25:58 to 10:21:54. A pair of exposures were taken with each grating, dithered by 0.4 arcsec, up to a total exposure time of 2071.622 s (see details in Table A.1). To optimize the detector noise performance, the NRSIRS2RAPID readout method was used.

The data processing and spectral extraction methodology (described in A) were identical to that used in other recent studies of TNOs observed through GTO Programs (see Emery et al. (2024) and Grundy et al. (2024) for a detailed description). We show in Figure 1 Chiron's reflectance spectrum. In Figure 2, we include the stack of several wavelength slices of the NIRSpec datacube in the 3.3 μm region (panel a) and one single slice at 3.29691 μm (panel b) for comparison.

3. Results

3.1. Spectral features

The combined spectrum within the range of 0.9–5.2 μm is shown in Figure 1. The continuum below 2.6 μm shows a blue slope that is rare in the population of TNOs and centaurs studied with Webb (Pinilla-Alonso et al. 2024; Emery et al. 2024; Grundy et al. 2024; Licandro et al. 2024). To compare it with the slope of 59 TNOs and centaurs observed with JWST/NIRSpec, we calculated the slope of the continuum from 0.9 to 1.2 μm (SIR'_1) and from 1.15 to 2.6 μm (SIR'_2), normalized at 1.175 μm (where both intervals overlap) following the definition by Pinilla-Alonso et al. (2024). This results in values of $SIR'_1 = -1.270 \pm 0.010$ and $SIR'_2 = -1.025 \pm 0.010$%/0.1 μm.

We detect two bands at 1.5 and 2.02 μm above 1.5- and 3.0-σ, respectively (Figures 1 and 3a). Although they have been attributed in the literature to water ice overtone and combination bands, we cannot rule out contributions from –OH, –NH, and –CH bands in complex organics, as is shown for water-ice-poor TNOs (Pinilla-Alonso et al. 2024). The broad absorption between 2.6 and 3.2 μm (Figure 3b) is consistent with the fundamental O–H stretching mode in water ice or refractory material, although N–H could also contribute in this region. The absence of the 3.1 μm Fresnel reflection peak, typically observed in TNOs and centaurs with evident water ice (Pinilla-Alonso et al. 2024), implies that any water ice present is predominantly in the amorphous state. Moreover, the unconfirmed 1.65 μm band (see Figure C.2a), traditionally used to detect crystalline water ice in icy bodies, further supports this conclusion.

The analysis of the full profile of the broad 3-μm absorption reveals additional unique characteristics for Chiron when compared to other centaurs (Licandro et al. 2024). As is shown in Figures 3b and 4b, we attribute the bands between 3.35 and 3.55 μm to the –CH and $–CH_3$ stretching and combination modes of aliphatic hydrocarbons. We consider ethane (3.47,

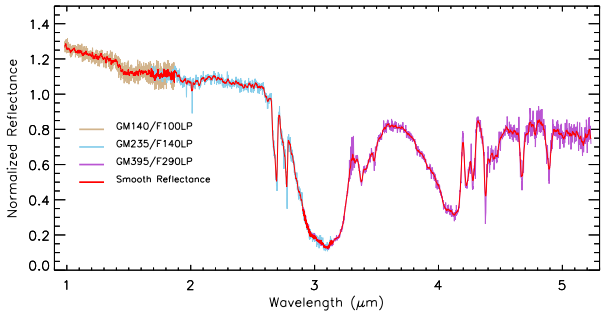

Fig. 1. Chiron's spectrum across the full NIRSpec spectral range with overplotted smoothed version in red. The smoothed version was calculated with a ten-point boxcar average.

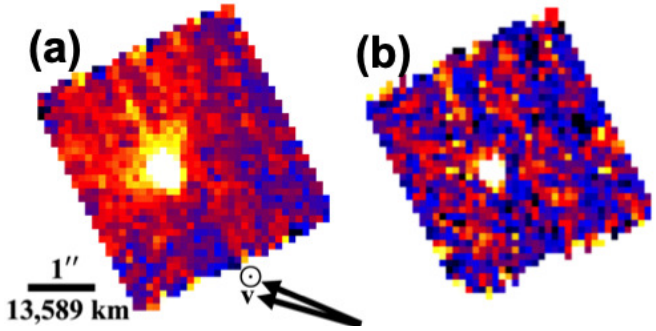

Fig. 2. (a) Stack of six NIRSpec slices at the emission peaks from 3.28975 to 3.31302 μm revealing extended emission around Chiron's nucleus, indicating a CH_4 coma. (b) Individual data cube slice at 3.29691 μm, in between emission peaks of CH_4 gas, shows no extension beyond a PSF (see Section 3.2 for details). Both (a) and (b) have the same sky plane dimensions and the projected directions of the Sun and velocity direction are shown.

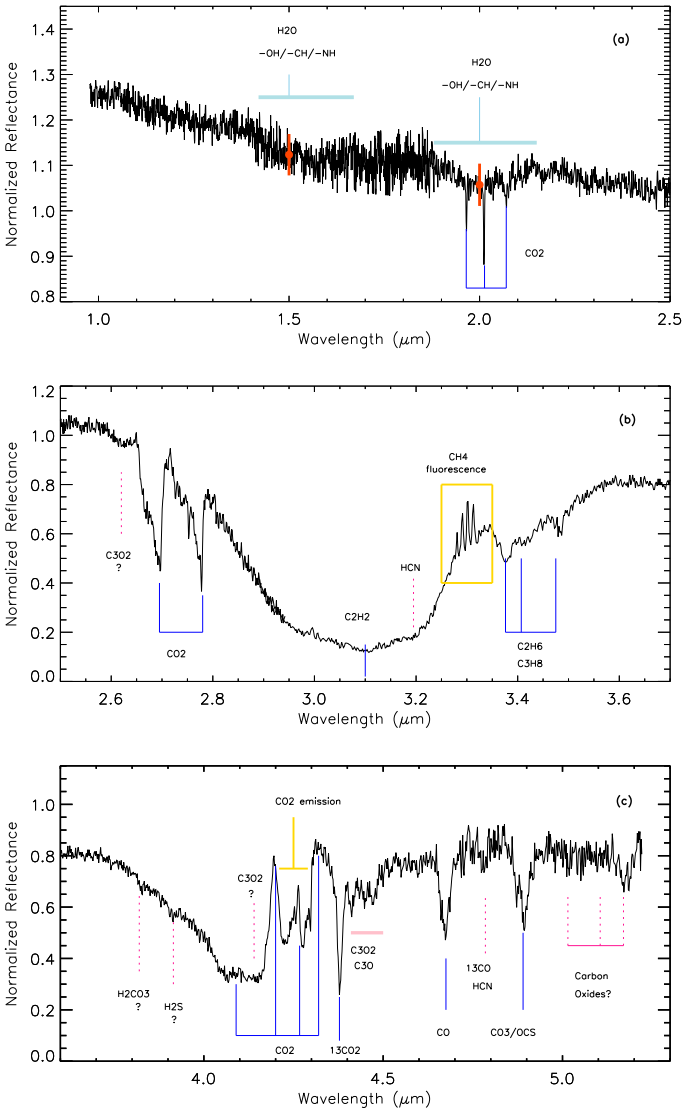

Fig. 3. Chiron's spectrum obtained with the G140M/F100LP (top), G235M/F140LP (middle), and G395M/F290LP (bottom) grisms of NIRSpec. Clear attributions for the absorption bands are signaled in solid blue lines and tentative ones in dotted pink lines. The red dots at 1.5 and 2.0 μm in the top panel represent the 1.5 and 3.0σ error bars, respectively, calculated with the standard deviation around the center of each band.

3.4, 3.36 μm) and propane (3.38, 3.48 μm) to be the best candidates. Relatively light hydrocarbons can form after irradiation of CH_4 mixed with H_2O (Hudson et al. 2014; Mifsud et al. 2023). Acetylene (C_2H_2) might be responsible for the dip at 3.1 μm corresponding to its ν_1 and ν_3 C-H stretching modes (Zhang et al. 2023), which are its most active modes in this wavelength range. Notably, we do not detect the 3.24-μm feature of ethylene (C_2H_4). None of these light hydrocarbons have been detected on centaurs before.

At $\lambda > 3.7$ μm, absorptions of –CO– molecules dominate the spectrum (see Figure 3c). The absorption at 4.09 μm and the two peaks at 4.2 and 4.3 μm are part of the fundamental antisymmetric stretching mode of CO_2, observed in TNOs but not in centaurs, and can be explained by the complex optical properties of this molecule. The 4.09-μm absorption is attributed by De Prá et al. (2024) to the Christiansen effect, which minimizes light scattering in spectral regions in which the real index of refraction of the ice matches that of the surroundings. Specifically, De Prá et al. (2024) show that the double-peaked shape of the 4.27-μm band is more evident when CO_2 is abundant and segregated, particularly in high-porosity regimes in which the CO_2 particles are surrounded by a vacuum with a refractive index of 1. The bands at 2.70 and 2.77 μm correspond, respectively, to the $\nu_1 + \nu_3$ and $2\nu_2 + \nu_3$ combinations of CO_2. These bands are much deeper than so-far observed in any TNO (see Figure C.1 and De Prá et al. 2024; Pinilla-Alonso et al. 2024), suggesting a significant surface abundance of CO_2, which is confirmed by the detection of the $2\nu_1 + \nu_3$, $\nu_1 + 2\nu_2 + \nu_3$, and $4\nu_2 + \nu_3$ combination bands of this ice at 1.966, 2.012, and 2.070 μm, respectively (Bernstein et al. 2005). The deep and sharp absorption at 4.39 μm corresponds to the $^{13}CO_2$ isotopologue, also present on CO_2–rich TNOs but not previously detected on centaurs (Licandro et al. 2024). Its right shoulder has a different shape from that seen in CO_2-rich TNOs, suggesting the presence of additional molecules absorbing between 4.4 and 4.5 μm (see Figures C.1 and C.2b and Appendix B for a tentative attribution).

At 4.68 μm, we identify the fundamental absorption of CO ice. Chiron's CO absorption has a symmetrical profile with no indication of the absorption at ~4.6 μm associated with cyanates or isocyanates detected on TNOs (Pinilla-Alonso et al. 2024) and Enceladus (Villanueva et al. 2023). The small absorption at 4.78 μm coincides with the ^{13}CO vibrational stretching mode of CO, identified in icy grain mantles of protostars (Boogert et al. 2002) but not previously detected on centaurs or TNOs. However, HCN is another possibility for this band (Figures 3c or C.2c). HCN could be connected to the presence of C≡N outgassing in previous observations of Chiron's coma (Bus et al. 1991).

The last strong absorption is a sharp band at 4.89 μm, with three possible attributions. Carbon trioxide (CO_3) is a common irradiation product of CO_2-dominated ices and has its sharp ν_1 mode (C=O stretch) at 4.895 μm, coinciding with the band in our spectrum. OCS has a strong band at 4.88–4.90 μm, depending on the ice mixture, somewhat broader than CO_3. OCS is one ingredient of protoplanetary ices (McClure et al. 2023) and it can also be formed by proton-irradiation of water-free or water-dominated ices containing CO or CO_2 as the carbon source and H_2S or SO_2 as the sulfur source (Ferrante et al. 2008). The OCS band is frequently blended with that of CO_3 in the presence of sulfur ices mixed with CO_2. In the spectrum of Chiron, the shape and the position of the band are compatible with the presence of both OCS and CO_3 (Figure C.2c). A third possible attribution to this band is the 4.84 μm of CO_2. However, this band is much weaker than the bands of OCS or CO_3. In fact, based on the band strength of these materials (Yarnall & Hudson 2022; Martín-Doménech et al. 2015), a 0.01 ratio OCS/CO_2 or of CO_3/CO2 would be largely enough to explain the strong 4.9 μm band on Chiron. Additionally, the band area ratio of the 2.7–4.9 μm bands in Chiron's spectrum (~4.5) is not compatible with the band area ratio in laboratory reflectances of pure CO_2 (~70–150), whereas it is in the order of the ratio for reflectances of irradiated CO_2 (~4.3–4.7), in which the band is attributed to CO_3 (for tentative detection of other ices based on minor absorption bands at 2.62, 3.82, 3.9, 4.45, and 5.27 μm, see Appendix B).

3.2. Gas species detection

We report the detection of emission features associated with two gas species in Chiron's atmosphere. From 3.25 to 3.4 μm, we observe at least eight emission peaks (see Figure 4b), aligning with the P and Q branches of the fluorescence emission of

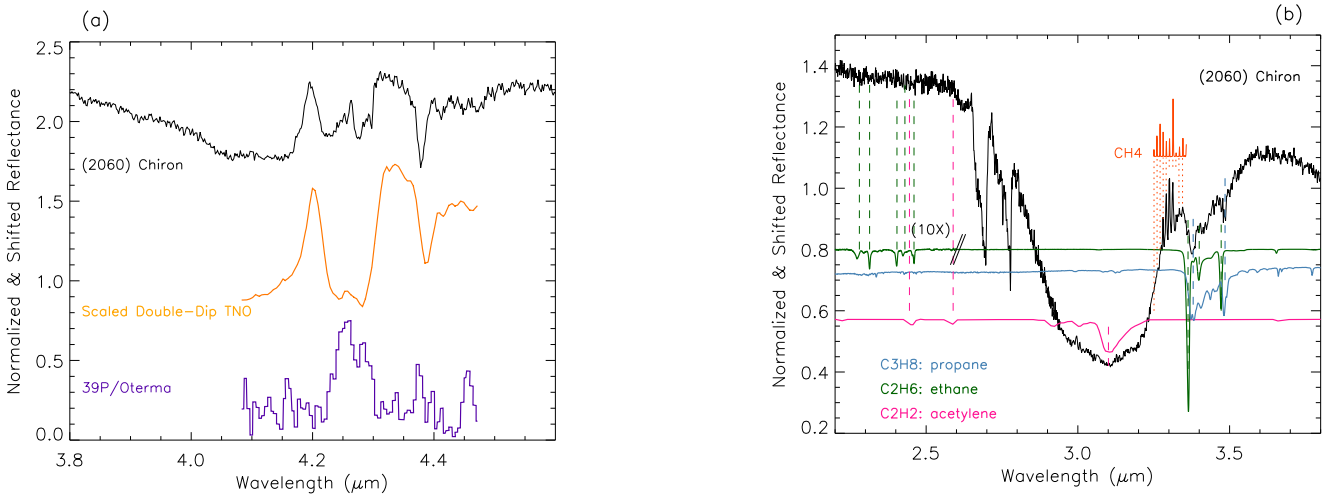

Fig. 4. (a) Chiron's CO_2 fundamental band, showing characteristics compatible with both the CO_2 absorption band in carbon-ice rich TNOs and with the CO_2 emission band in an active centaur, 39P/Oterma. (b) Chiron's spectrum compared with reflectances of some light hydrocarbons, including the comparison with the CH_4 fluorescent spectrum.

methane. Also, at the center of the fundamental band of CO_2 we report the presence of an emission peak, corresponding to CO_2 gas in the coma (Figure 4a). Our spectrum does not show a clear detection, above the noise, of CO emission around 4.67 μm; hence, CH_4 and to a lesser extent CO_2 dominate the gas phases in the coma.

Although the observing mode was not optimized for the detection of extended emission, we clearly show a coma around Chiron's nucleus (Figure 2a). This panel shows the stack of six image slices in CH_4 emission peaks at 3.28975, 3.29154, 3.30049, 3.30228, 3.31123, and 3.31302 μm shows clear extended surface brightness around the nucleus' point source detection (Figure 2a). An image slice at 3.29691 μm (between CH_4 emission peaks) is consistent with that of a point source (Figure 2b). The coma presents a fan shape extending over ∼180°, roughly centered near the position angle of the projected Sun direction, compatible with gas production on or close to the subsolar point. Two brightness levels can be seen in the coma, one brightest around the non-resolved nucleus and a fainter one extending tens of thousands of kilometers toward the limits of the image. The observed structure is independent of which CH_4 emission peak slices are used to generate the stacked image. No coma is evident around the CO_2 emission region. A detailed analysis of the structure of the coma is out of the scope of this Letter and part of a second manuscript.

4. Discussion

Chiron's distinct attributes, including activity at aphelion and a ring of material evolving on relatively short timescales (Sickafoose et al. 2023; Ortiz et al. 2023), pose a challenge to associating the spectral absorptions and emissions presented in this work with specific parts of Chiron; that is, the surface ice, ring material, or icy particles in the coma. However, this complexity could explain the unique characteristics of Chiron's spectrum, deviating from the spectral groups defined based on Webb observations of TNOs and other centaurs (Licandro et al. 2024). The deep CO_2/CO absorptions and the presence of –CH stretching bands at ∼3.3 μm resemble the main characteristics of double-dip type TNOs, making Chiron the first centaur with a double-dip type spectrum above 1.2 μm. A significant unresolved issue, discussed by Licandro et al. (2024), is the absence of double-dip type centaurs, the most prevalent type in the JWST-TNOs sample. The authors propose that double-dip TNOs, rich in CO_2 and CO ices, may undergo evolution into the shallow-type centaurs, characterized by dominance in dust or refractory material, after entering the giant planet region. Therefore, if Chiron's nucleus were a double dip recently injected into the planetary region, it holds the potential to serve as a representative specimen for the early surface thermal evolution within this class of Solar System bodies, rich in carbon volatiles. The investigation into the secular evolution of Chiron's nucleus spectrum emerges as a crucial avenue of future exploration.

The distinctive blue continuum below 1.2 μm sets Chiron apart from both TNOs and active centaurs, the latter reported to be bluer than inactive centaurs but still exhibiting a reddish hue (Jewitt 2009). This blue color suggests a surface composition lacking in red complex organics. If Chiron's surface once harbored such organics, as is indicated by the reddish slope observed in the visible spectrum of double-dip type TNOs, their influence on the spectral reddening appears to have been mitigated, possibly by a layer of dust and ices or by the presence of a bluer coma. Indeed, a blue coma has been documented for another active centaur, 174P/Echeclus, despite its red nucleus (Seccull et al. 2019). The authors attribute this coloration to the unique composition of 174P's coma, hinting at a prevalence of blue dust particles. Similarly, a blue coma in comet 9P/Tempel 1 has been attributed to water-ice-rich grains (Beer et al. 2009; Fernández et al. 2007). Beyond compositional factors, scattering effects (Jewitt 2009), grain size, and viewing geometry can further obscure the red color in the visible. Taking all these variables into account, Filacchione et al. 2020 propose that color variations observed in comet 67P/Churyumov Gerasimenko along its orbit are indicative of an orbital water-ice cycle driven by solar heating. It is conceivable that Chiron's blue coloration similarly reflects a complex cycle in which changes in surface, ring, and coma compositions over time contribute to the observed color of the continuum.

Longward of 2.5 μm, the spectrum displays a rich collection of spectral features. Specifically, we detect fluorescence emission of CH_4 but not absorption bands associated with this ice. For CO_2, less volatile than methane, we observe a combination of gas and ice features. The existence of a reservoir of volatile ices on or near Chiron's surface, revealed for the

first time by this JWST spectrum, is compatible with what is known about the body's physical state. First, dynamical models suggest that Chiron is a recent addition to the planetary region (Levison & Duncan 1994; Dones et al. 1996), which would imply a low dust-to-ice ratio for its surface composition (Melita & Licandro 2012). Second, Chiron is a large centaur orbiting the Sun at heliocentric distances exceeding 8.5 au. Thus, throughout its orbit its equilibrium temperature remains below 140 K (Prialnik & Jewitt 2022), the temperature at which water ice transforms into the cubic form leading to a pulse in the release of trapped volatiles. In particular, the survival of methane ice accessible for sublimation on Chiron requires that it be mixed or trapped in water ice, probably below the surface, which would be consistent with the lack of ice CH_4 bands in the spectrum. Crystallization of water ice has traditionally been claimed to be a triggering mechanism of activity. However, this process is not very efficient at large heliocentric distances (Guilbert-Lepoutre 2012; Davidsson 2021). Consequently, a mechanism more suitable for the recurrent activity of Chiron close to aphelion has to be invoked.

Recent laboratory investigations into the desorption of CH_4 in amorphous water ice (AWI), with or without the presence of a refractory mantle (Tamai et al. 2023), reveal a temperature desorption profile with three peaks at 60, 140, and 160–180 K, corresponding to three different processes. The first peak, the low-temperature one, can be attributed to the desorption of methane during a change in the AWI from a high-density phase to a low-density one aligning with the estimated temperature of Chiron during JWST observations (61 K). If the temperature of the ice is steadily increased, continuous desorption at a lower rate occurs due to the reorganization of AWI, which causes a change in the size and shape of the porous structure upon heating (Cazaux et al. 2015). In the final stages, corresponding to temperatures found around 10 au, the crystallization of AWI is expected to become more efficient and increasingly affect the release of volatile species. However, because of Chiron's large perihelion compared to other active centaurs (the median perihelion distance of active centaurs is 5.9 au; Jewitt 2009), we could expect some CH_4 to be preserved, trapped in the AWI in the inner layers, to be released in successive cycles around the Sun.

The discovery of additional molecules opens a new avenue to the understanding of the surface of centaurs, in particular the detection of less volatile species present in laboratory experiments as byproducts of the irradiation of methane, pure or mixed with water; namely, C_2H_6, C_2H_2, and C_3H_8. While ethane and ethylene are common in comets (Lippi et al. 2021) and abundant on Sedna (Emery et al. 2024), the presence of these light hydrocarbons on centaurs is unprecedented. The case for propane is even more remarkable as it has never been detected in the ice phase on small bodies, although its detection in the coma of 67 P (Schuhmann et al. 2019) might imply its presence in the nucleus. The lack of detection of other irradiation products such as CH_3OH, detected in TNOs, or C_2H_4, detected in Sedna, provides valuable insights into the relative abundances of irradiation products. The coexistence on the surface of -CH- molecules with very different vapor pressures opens the floor for numerical models of the escape rate of these volatiles at the specific temperature along Chiron's orbit. Ethane and acetylene can either be inherited from cold interstellar and outer protoplanetary disk regions where TNOs formed (Hudson et al. 2014), or formed much later as radiation products of methane (Bennett et al. 2006) under conditions similar to Chiron's environment. The simultaneous detection of irradiation byproducts of CO_2 and CO, such as CO_3 and other oxides, would support the second scenario. The interplay of -CH- and -CO- irradiation products results in the formation of carbon complex molecules such as H_2CO, CH_3CHO, or CH3COOH. The fact that we do not detect them on Chiron's surface could be an indication of some physical or temporal separation between the reservoirs of CH_4 and CO_2.

Finally, the emission of CO_2, vastly less volatile than CO, in the absence of CO emission, poses a challenge to an explanation solely based on sublimation on the surface of Chiron's nucleus. Previously, observational studies reported the detection of CO gas on Chiron at 8.5 au (Womack & Stern 1999). CO ice is now detected in Chiron's spectrum at a much larger distance of 18 au. At the lower temperatures Chiron experiences in its orbit, the relative volatility of the various ices identified can vary significantly (even methane and acetylene). Therefore, fully understanding the loss and transport of these species presents a complex challenge. To understand why Chiron's spectrum shows CO_2 and CH_4 gas while CO is in the ice form, it may be necessary to explore intricate scenarios in which the absorption and emissions of different materials originate in distinct reservoirs on Chiron, each possessing unique physical or chemical properties. One conceivable scenario involves ice absorptions originating from the nucleus at an equilibrium temperature of ∼60 K. Additionally, emission of specific ices on the nucleus may occur around the subsolar point, at which the temperature reaches ∼90 K. Sublimation being restricted to a localized region is supported by the fan-shaped images of the coma. A second source of sublimation could be the dust in the coma, which could elevate the temperature of ice particles. In both scenarios, it is plausible that the amount of CO ice available in that source area was limited and may now be exhausted. Consequently, CH_4 and CO_2, being less volatile than CO, would persist as the dominant ices undergoing sublimation. As a result, the ejection of CO particles from Chiron's subsurface would have ceased or become minimal.

5. Conclusions

Our study marks the first detection of CH_4 and CO_2 active outgassing and coma emission on any active object in the Solar System at heliocentric distances of ∼18 au. It also shows unprecedented detections of several ices of different volatilities in the centaur population that contribute valuable insights into the primordial state of the outer Solar System. The coexistence of these gases with the ice phase of CO challenges the current paradigm of activation mechanisms for comets and centaurs, and raises new questions that could be addressed by future comprehensive investigations into the gas and ice components. The reflectance spectrum of Chiron reveals a complex nature that could be a manifestation of the coexistence of a nucleus, debris ring, and coma. The presence of irradiation byproducts of CH_4, CO_2, and CO in both reducing (e.g., C_2H_6) and oxidizing (e.g., CO_3) conditions adds an extra level of complication. Exploration of secular variations in Chiron's spectrum, and careful simulation of volatile stability and escape rates from Chiron's surface, could help determine the triggering mechanism on this peculiar centaur and the alteration degree of its surface under irradiation.

Acknowledgements. NPA acknowledges the Ministry of Science, Innovation, and Universities (MICIU) in Spain and the State Agency for Research (AEI) for funding through the ATRAE program, project ATR2023-145683. JIL acknowledges support from NASA-JWST to project GTO-1273 (PI. J. I. Lunine). RB and EH acknowledge support from the CNES-France (JWST mission). JL acknowledges support from the Agencia Estatal de Investigacion del Ministerio de Ciencia e Innovacion (AEI-MCINN) under grant "Hydrated Minerals and Organic Compounds in Primitive Asteroids" with reference PID2020-120464GB-100. We thank O. Harrington-Pinto for providing the spectrum of 39P/Oterma. We

thank E. Palumbo and D. Mifsud for providing the necessary data files from their laboratory work. As we explore a new wavelength range, the significance of collaboration between observers and laboratory scientists is clearer than ever.

References

Ahrens, C., Meraviglia, H., & Bennett, C. 2022, Geosciences, 12, 51
Beer, E., Wooden, D. H., & Schulz, R. 2009, in Deep Impact as a World Observatory Event: Synergies in Space, Time, and Wavelength, eds. H. U. Käufl, & C. Sterken, 59
Bennett, C. J., Jamieson, C. S., Osamura, Y., & Kaiser, R. I. 2006, ApJ, 653, 792
Bernstein, M. P., Cruikshank, D. P., & Sandford, S. A. 2005, Icarus, 179, 527
Bieler, A., Altwegg, K., Balsiger, H., et al. 2015, Nature, 526, 678
Böker, T., Beck, T. L., Birkmann, S. M., et al. 2023, PASP, 135, 038001
Boogert, A. C. A., Blake, G. A., & Tielens, A. G. G. M. 2002, ApJ, 577, 271
Bus, S. J., A'Hearn, M. F., Schleicher, D. G., & Bowell, E. 1991, Science, 251, 774
Bushouse, H., Eisenhamer, J., Dencheva, N., et al. 2024, https://doi.org/10.5281/zenodo.6984365
Calmonte, U., Altwegg, K., Balsiger, H., et al. 2016, MNRAS, 462, S253
Cazaux, S., Bossa, J. B., Linnartz, H., & Tielens, A. G. G. M. 2015, A&A, 573, A16
Cochran, A. L., Levasseur-Regourd, A.-C., Cordiner, M., et al. 2015, Space Sci. Rev., 197, 9
Davidsson, B. J. R. 2021, MNRAS, 505, 5654
De Prá, M. N., Hénault, E., Pinilla-Alonso, N., et al. 2024, Nat. Astron., https://doi.org/10.1038/s41550-024-02276-x
Dobson, M. M., Schwamb, M. E., Fitzsimmons, A., et al. 2021, Res. Notes Am. Astron. Soc., 5, 211
Dones, L., Levison, H. F., & Duncan, M. 1996, ASP Conf. Ser., 107, 233
Emery, J. P., Wong, I., Brunetto, R., et al. 2024, Icarus, 414, 116017
Fernández, Y. R., Lisse, C. M., Kelley, M. S., et al. 2007, Icarus, 187, 220
Ferrante, R. F., Moore, M. H., Spiliotis, M. M., & Hudson, R. L. 2008, ApJ, 684, 1210
Ferrari, B. C., Slavicinska, K., & Bennett, C. J. 2021, Acc. Chem. Res., 54, 1067
Filacchione, G., Capaccioni, F., Ciarniello, M., et al. 2020, Nature, 578, 49
Fornasier, S., Lellouch, E., Müller, T., et al. 2013, A&A, 555, A15
Gerakines, P. A., & Moore, M. H. 2001, Icarus, 154, 372
Gerakines, P. A., Yarnall, Y. Y., & Hudson, R. L. 2022, MNRAS, 509, 3515
Grundy, W., Wong, I., Glein, C., et al. 2024, Icarus, 411, 115923
Guilbert-Lepoutre, A. 2012, AJ, 144, 97
Hudson, R. L., & Gerakines, P. A. 2018, ApJ, 867, 138
Hudson, R., Ferrante, R., & Moore, M. 2014, Icarus, 228, 276
Huntress, W. T., Jr., Allen, M., & Delitsky, M. 1991, Nature, 352, 316
Jakobsen, P., Ferruit, P., Alves de Oliveira, C., et al. 2022, A&A, 661, A80
Jewitt, D. 2009, AJ, 137, 4296
Johnson, R. E., Carlson, R. W., Cooper, J. F., et al. 2004, in Jupiter. The Planet, Satellites and Magnetosphere, eds. F. Bagenal, T. E. Dowling, & W. B. McKinnon, 1, 485
Lazzaro, D., Florczak, M. A., Angeli, C. A., et al. 1997, Planet. Space Sci., 45, 1607
Levison, H. F., & Duncan, M. J. 1994, Icarus, 108, 18
Licandro, J., Pinilla-Alonso, N., Holler, B., et al. 2024, Nat. Astron., accepted, https://doi.org/10.21203/rs.3.rs-3606680/v1
Lippi, M., Villanueva, G. L., Mumma, M. J., & Faggi, S. 2021, AJ, 162, 74
Luu, J. X., Jewitt, D. C., & Trujillo, C. 2000, ApJ, 531, L151
Marcialis, R. L., & Buratti, B. J. 1993, Icarus, 104, 234
Martín-Doménech, R., Manzano-Santamaría, J., Muñoz Caro, G. M., et al. 2015, A&A, 584, A14
Mastrapa, R. M. E. 2010, Optical Constants and Lab Spectra of Water Ice V1.0 NASA Planetary Data System, id. EAR-X-I0065-5-ICESPEC-V1.0
McClure, M. K., Rocha, W. R. M., Pontoppidan, K. M., et al. 2023, Nat. Astron., 7, 431
Melita, M. D., & Licandro, J. 2012, A&A, 539, A144
Mifsud, D. V., Herczku, P., Sulik, B., et al. 2023, Atoms, 11, 19
Moore, M. H., Ferrante, R. F., Moore, W. J., & Hudson, R. 2010, VizieR Online Data Catalog: J/ApJS/191/96
Ortiz, J. L., Duffard, R., Pinilla-Alonso, N., et al. 2015, A&A, 576, A18
Ortiz, J. L., Pereira, C. L., Sicardy, B., et al. 2023, A&A, 676, L12
Palumbo, M. E., Leto, P., Siringo, C., & Trigilio, C. 2008, ApJ, 685, 1033
Peeters, Z., Hudson, R. L., Moore, M. H., & Lewis, A. 2010, Icarus, 210, 480
Pinilla-Alonso, N., Brunetto, R., De Prá, M., et al. 2024, Nat. Astron., accepted, https://doi.org/10.21203/rs.3.rs-5485727/v1
Prialnik, D., & Jewitt, D. 2022, arXiv e-prints [arXiv:2209.05907]
Rauscher, B. J. 2024, PASP, 136, 015001
Schuhmann, M., Altwegg, K., Balsiger, H., et al. 2019, A&A, 630, A31
Seccull, T., Fraser, W. C., Puzia, T. H., Fitzsimmons, A., & Cupani, G. 2019, AJ, 157, 88
Sickafoose, A. A., Levine, S. E., Bosh, A. S., et al. 2023, Planet. Sci. J., 4, 221
Tamai, C., Maté, B., Cazaux, S., & Satorre, M. Á. 2023, A&A, 675, A47
Tholen, D. J. 1988, Minor Planet. Bull., 15, 35
Villanueva, G. L., Hammel, H. B., Milam, S. N., et al. 2023, Nat. Astron., 7, 1056
Womack, M., & Stern, S. A. 1999, Sol. Syst. Res., 33, 187
Yarnall, Y. Y., & Hudson, R. L. 2022, ApJ, 931, L4
Zhang, C., Zhu, C., Turner, A. M., et al. 2023, Sci. Adv., 9, eadg6936

Table A.1. Observation Details [1]

Grating/Filter	Date UT	Start Time UT	t_{int} [2] s
G140M/F100LP	12 Jul 2023	09:25:58	291.8
G235M/F170LP	12 Jul 2023	09:39:50	729.4
G395M/F290LP	12 Jul 2023	10:00:44	1050.4

[1] t_{init}: integration time per dither
[2] r (heliocentric distance): 18.771 au; Δ (distance to observer): 18.747 au; phase angle, Sun-target-JWST: 3.140

Appendix A: Reduction of the data

The fully calibrated spectral data cubes, containing stacks of 2D sky-projected wavelength slices, were constructed by running the raw uncalibrated data files through the first two stages of Version 1.13.4 of the official JWST calibration pipeline (Bushouse et al. 2024), with all relevant calibration reference files drawn from context jwst_1188.pmap of the JWST Calibration Reference Data System. This version of the JWST calibration pipeline includes a readnoise correction step based off the NSClean routine described in (Rauscher 2024). This step of the pipeline, which is not run by default, was turned on when processing the data locally. To extract the spectrum, we utilized the empirical point spread function (PSF) fitting methodology that has been applied to other JWST observations of small bodies (Grundy et al. 2024; Emery et al. 2024). At each wavelength in the spectral data cube, the local template PSF was constructed by median-averaging the 10 adjacent slices in both directions, subtracting the background level, and normalizing the template to a unit sum. Then, this template PSF was fit to the central wavelength slice with a scaling factor and a constant background level. The spectrum presented in this paper was extracted from a 5x5 pixel square aperture centered on Chiron's centroid, with the background region defined as all pixels external to the 11x11 pixel box around Chiron. This PSF fitting process was applied to each dithered exposure individually, with the final combined spectrum derived by cleaning 5σ outliers in the individual spectra using a 20-pixel-wide moving median filter and averaging each dither pair together.

Appendix B: Other bands

There are several small bands identified in the spectrum that could be explained by irradiation products of CO_2 or CO, pure or mixed with water ice. Carbon suboxide (C_3O_2, at 2.671 and 4.46 μm Ferrante et al. (2008) see Figures 3b-c and C.2b) has been proposed by (Huntress et al. 1991) as a source of CO and C emission in cometary comae. This material has a NIR spectrum that is sensitive to the effects of dilution in a molecular matrix. The extreme values of the peak position for the ν_3 C_3O_2 features cover the 4.43 to 4.59 μm and the width varies greatly, from only 0.02 to 0.2 μm. We find this is a good candidate for the second absorption on the right of the $^{13}CO_2$ band (see Figure C.2b).

H_2CO_3 (carbonic acid) is considered a tentative candidate for the small band at 3.82 μm, attributed to the O–H stretching, the strongest in the wavelength range covered by this spectrum. This acid is a notable byproduct of low-temperature photo- and ion-radiation of H_2O:CO_2 ice (Peeters et al. 2010). Notably, carbonic acid exhibits a lower vapor pressure than both H_2O and CO_2, suggesting potential stability on a planetary surface, given that the molecule is protected from elevated temperatures and reactions with NH_3 or other bases. While claims of carbonic acid detection have been made for celestial bodies such as Callisto Johnson et al. 2004, no such detection has been reported in comets Ahrens et al. 2022.

Finally, other oxides such as C_3O, also a candidate for the 4.46 μm band as discussed above, and C_2O could be causing bands in the 4 - 5.3 μm range. Many high-order carbon oxides have been observed as products of proton irradiation of CO_2 (Ferrari et al. 2021) or CO–rich ices (Gerakines & Moore 2001) in the laboratory although no detection has been claimed for small icy objects. In particular, Bieler et al. 2015 proposes carbon oxides as the origin of the O_2 detected in the coma of 67P/Churyumov–Gerasimenko. At low irradiation doses, these ices could remain stable which would be compatible with a young-icy surface like the one that we observe for Chiron.

The weak 3.91 μm band could be associated to the S–H stretching modes in H_2S or as a thiol function (–SH) in more complex molecules (Hudson & Gerakines 2018). H_2S has been detected in, at least, 10 comets (Cochran et al. 2015)and CH_3SH in one, 67/P (Calmonte et al. 2016). Hydrogen sulfide (H_2S) has also tentatively associated with a similar band in some TNOs, principally those with red colored spectrum below 1.2 μm and a chemically evolved surface (Pinilla-Alonso et al. 2024).

For the data cube slices where extended emission due to the presence of a CH_4 coma is observed, the PSF-fitting spectral extraction technique provides an underestimate of the true flux, as the inherent morphology of those data cube slices is not represented solely by the PSF (see Figure 2 a and b). For the initial assessment of the Chiron spectrum we are presenting here we are only concerned with the presence of the extended emission features and not on the precise CH_4 production rate measurements, so the PSF-fitting approach minimally impacts our results.

To obtain the reflectance spectrum, the irradiance spectrum of Chiron was divided by the analogously extracted spectrum of the solar analog star P330E (obtained as part of JWST Calibration Program 1538). The aperture size in the stellar spectrum extraction was chosen to match the corresponding size used for the Chiron observation. Chiron's reflectance spectrum is shown in figure 1 normalized at 2.6 μm for a better comparison with spectra of other TNOs and centaurs obtained with Webb.

Appendix C: Implication of a fan-shaped coma

The fan-shaped CH_4 gas coma morphology directed to the northeast, on the sunward side of the nucleus, suggests a localized source on or near Chiron's surface that is responding directly to the insolation. The lack of a circularly symmetric extended emission centered on the nucleus' location due to the CH_4 fluorescence suggests that the source of the CH_4 gas coma is not from an extended icy-grain halo surrounding Chiron.

Further evidence against an icy-grain coma source for the CH_4 emission is the lack of extended emission present in data cube slices at wavelengths just short of and longward of the CH_4 emission band (see Figure 2b), indicating the lack of a corresponding icy-grain coma. If the source of the CH_4 gas molecules was due to sublimation from icy grains in an extended coma source one would expect to detect a corresponding surface brightness outside of the CH_4 emission band due to the presence of this icy-grain coma material.

Table B.1. Band detections and corresponding attribution on Chiron's Spectrum. See 3.1 and B for details.

λ (μm)	ν (cm^{-1})	Detection	Species	Attribution
1.4–1.7	7143–5882	F	H_2O, –OH (tholins)	M
1.97, 2.01, 2.07	5076, 4975, 4831	F	CO_2	F
1.93–2.13	5181–4695	F	H_2O, –OH (tholins)	M
2.62	3817	F	C_3O	T
2.69, 2.775	3717.5, 3604	F	CO_2	F
3.095	3231	F	H_2O	F
3.193	3132	T	HCN	F
3.279, 3.290, 3.300, 3.313	3048,3039.5,3030,3018	F	CH_4	F[1]
3.375,3.40,3.483	2963,2971,2871	F	C_2H_6,C_3H_8	M[2]
3.825	2614	T[3]	H_2CO_3	T
3.9	2564	T[3]	H_2S	T
4.1–4.3	2439–2326	F	CO_2	F
4.15	2409	F	C_3O_2	T
4.23–4.29	2364–2331	F	CO_2	F[4]
4.378	2284	F	$^{13}CO_2$	F
4.396–4.488	2275–2228	F	C_3O_2/C_3O	T/M
4.673	2140	F	CO	F
4.78	2092	F	^{13}CO/HCN	M
4.89	2045	F	CO_3/OCS	M
5.016–5.25	1994–1905	T	Carbon Oxides	T

Detections or Attributions F = Firm; T = tentative; M = multiple possible contributions
(1) Fluorescent Emission
(2) –CH Aliphatic stretching, light hydrocarbons
(3) Confirmed by GO–2 Webb DDT observations in different epoch (personal communication)
(4) Ice absorption & emission from CO_2 gas in the coma

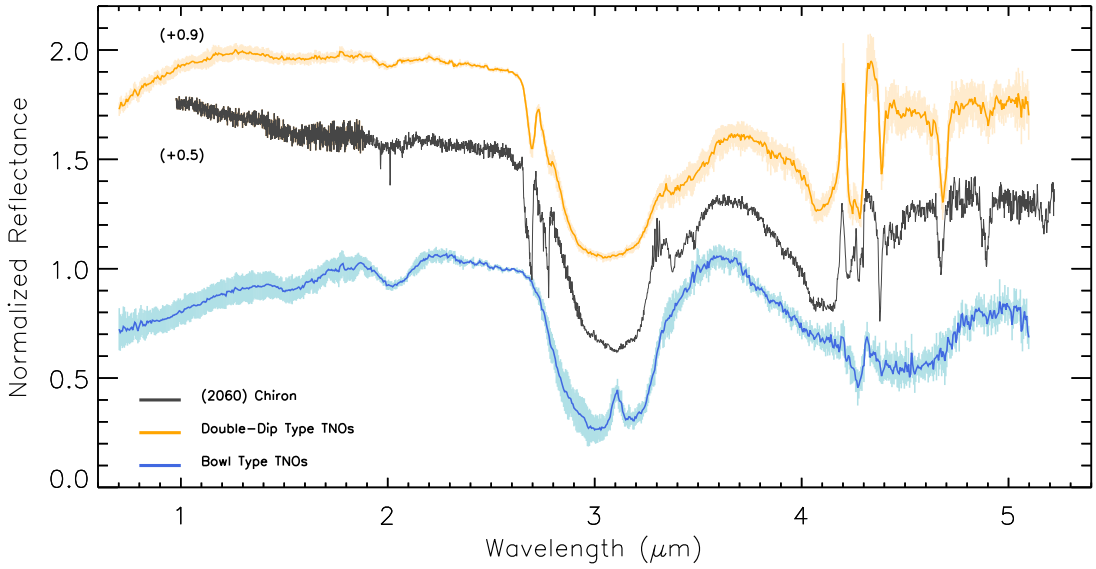

Fig. C.1. Spectrum of Chiron over the full spectra range covered by NIRSpec and the medium resolution grisms compared with the Bowl and double-dip type TNOs.

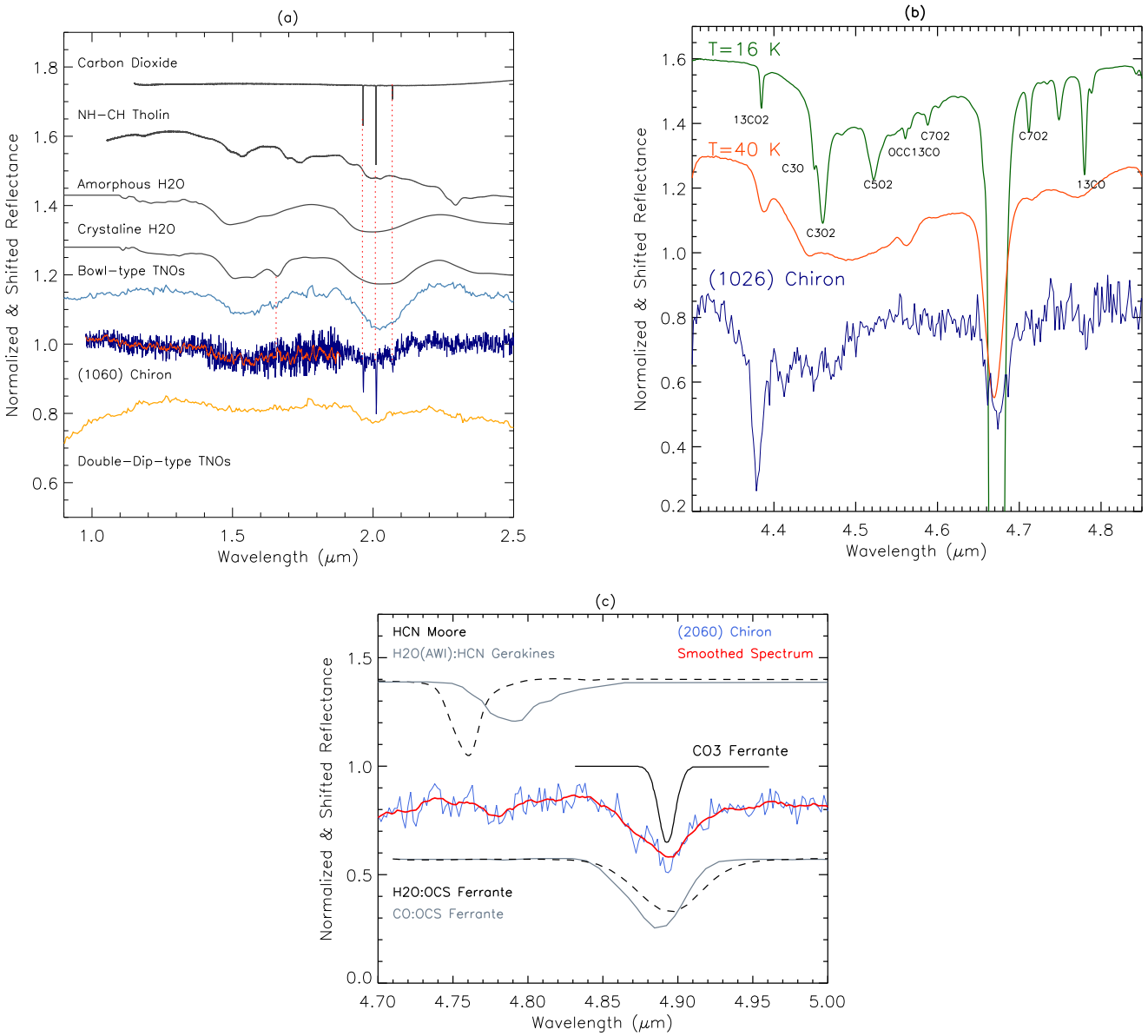

Fig. C.2. Ice detections in Chiron's spectrum. **(a)** Chiron's spectrum compared to the median of the Bowl- and double-dip type TNOs (Pinilla-Alonso et al. 2024). We also include the reflectance spectrum of amorphous and crystalline water ice (Mastrapa 2010), CO_2 (Henault personal communication), and tholins formed from irradiation -NH and -CH ices (Henault personal communication). The three colored reflectances have been divided by their continuum between 1.1 and 2.5 μm for a better visual comparison of the 1.5 and 2.0 μm absorption bands. Chiron's smooth spectrum appears in red in the G140M/F100LP (0.97–1.89 μm) wavelength range to better compare with the profile of the amorphous and crystalline water ice band at 1.52 μm. **(b)** Chiron's spectrum compared to the spectrum of the irradiation products of pure CO at 16 and 40 K from (Palumbo et al. 2008). **(c)** Chiron's spectrum compared with reflectance of HCN pure (Moore et al. 2010) and mixed with H_2O (Gerakines et al. 2022), CO_3 (Ferrante et al. 2008) and OCS (Ferrante et al. 2008). All the reflectances have been rescaled and shifted vertically for clarity.